

---

# A SELF-EXPLAINABLE MODEL OF LONG TIME SERIES BY EXTRACTING INFORMATIVE STRUCTURED CAUSAL PATTERNS \*

---

**Ziqian Wang**

Department of Automation  
Tsinghua University  
Beijing, China

wangziqi24@mails.tsinghua.edu.cn

**Yuxiao Cheng**

Department of Automation  
Tsinghua University  
Beijing, China

cyx22@mails.tsinghua.edu.cn

**Jinli Suo**

Department of Automation  
Tsinghua University  
Beijing, China

jlsuo@tsinghua.edu.cn

## ABSTRACT

Explainability is essential for neural networks modeling time series data, yet most existing explainable artificial intelligence (XAI) techniques generate point-wise importance scores that overlook intrinsic temporal semantics such as trends, cycles, and abrupt regime changes. This limitation obscures human interpretation and weakens trust in long-sequence models. To address these issues, we establish four desiderata for interpretable time-series modeling—temporal continuity, pattern-centricity, causal disentanglement, and faithfulness to the inference process—and propose EXCAP (EXplainable Causal Aggregation Patterns), a unified framework satisfying all four. EXCAP integrates an attention-based segmenter that extracts continuous temporal patterns, a causally disentangled decoder guided by a pre-trained causal graph, and a latent aggregation loss that enforces separability and stability in the representation space. Theoretical analysis demonstrates that EXCAP guarantees Lipschitz-continuous explanations over time, bounded error under causal mask perturbations, and improved latent-space stability. Comprehensive experiments on classification and forecasting benchmarks confirm that EXCAP outperforms state-of-the-art XAI methods in both predictive accuracy and interpretability, producing temporally coherent and causally grounded explanations. These results indicate that EXCAP provides a principled and scalable framework for faithful and interpretable modeling of long-horizon time-series, with direct relevance to decision-critical domains such as healthcare and finance.

**Keywords** Explainable AI, Time-series modeling, Causal representation learning, Interpretable deep learning

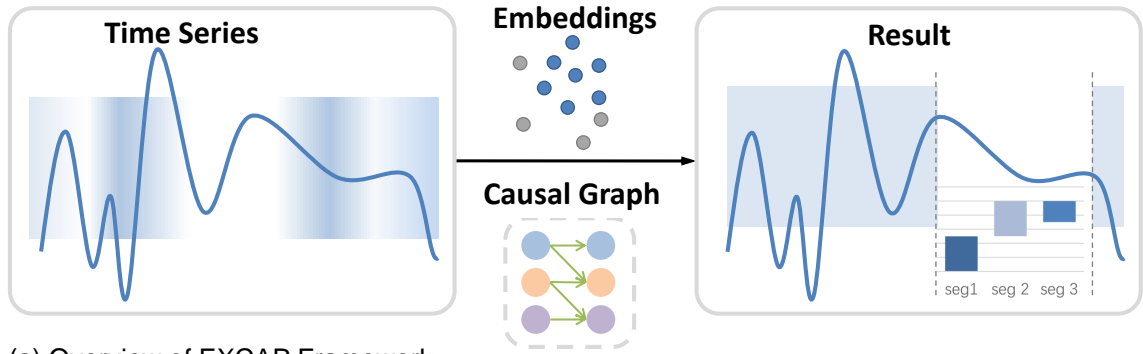
## 1 Introduction

Building explainable artificial intelligence (XAI) models is essential to enhance trust and accountability in machine-assisted decision making, particularly in high-stakes domains such as medicine, finance, and transportation [1, 2]. Time series data play a pivotal role in these domains, as exemplified by predicting sepsis onset from physiological signals in intensive care units [3] or forecasting stock market volatility [4]. Despite rapid progress in deep learning, most XAI methods still produce point-wise or feature-wise importance scores that work well for static inputs (e.g., images) but are inadequate for temporally dependent data, where trends, cycles, and abrupt regime shifts are fundamental. These approaches often fail to capture long-range dependencies and to uncover causal relationships underlying model predictions [5]. Recent attempts to leverage large language models (LLMs) for time-series reasoning [6] have provided intuitive, natural-language explanations, yet they remain post hoc approximations that do not necessarily reflect the model’s internal inference process.

A practical explainable time-series model should extract task-relevant patterns that integrate *temporal*, *spectral*, and *causal* structures [7, 8, 9, 10]. To this end, we identify four fundamental desiderata for interpretable temporal modeling: (i) **Continuity**, ensuring smooth variation of explanations along time; (ii) **Pattern-centricity**, associating attributions with coherent motifs such as peaks, trends, or state transitions; (iii) **Causal disentanglement**, isolating explanatory

---

\*Preprint. This version: 2025. Available at arXiv:XXXX.XXXXX.



(a) Overview of EXCAP Framework

Method	Continuity on time dim.	Pattern centric	Causal Disentanglement	Faithful to decision process
Attention-based	✓	✓	×	△
Causal-based	×	×	✓	✓
Post-hoc	×	×	×	△
EXCAP (Ours)	✓	✓	✓	✓

✓: Supported, × Not Supported, △: Partially Supported

(b) Comparison of Methodological Properties Across Interpretation Approaches

Figure 1: **Overview and comparative positioning of EXCAP.** (a) The proposed EXCAP framework extracts temporally and causally structured representations. (b) Qualitative comparison of interpretability properties across representative approaches.

rather than merely correlative factors; and (iv) **Faithfulness**, preserving consistency between the explanation and the model’s internal reasoning.

As summarized in Fig. 1(b), commonly used post hoc techniques such as LIME and SHAP [11, 12] provide feature-level relevance scores but lack temporal continuity and pattern-level semantics. Attention-based models (e.g., [13]) yield smoother attributions but offer limited causal interpretability. Recent works including BasisFormer [14], PatchX [8], and smoothed-SHAP variants [15] improve local pattern discovery and attribution stability, yet they struggle to jointly ensure temporal coherence and causal grounding. Conversely, causal discovery frameworks such as PCMCI [16] and CausalConceptTS [9] reveal directed dependencies across variables but overlook temporally meaningful motifs. Existing approaches thus meet only a subset of the desiderata, motivating the need for a unified framework that bridges temporal, causal, and semantic interpretability.

To address these limitations, we propose **EXCAP (EXplainable Causal Aggregation Patterns)**, a unified framework that provides faithful and semantically coherent explanations for multivariate time series. As shown in Fig. 1(a), EXCAP integrates three key components: (i) an attention-based segmenter that adaptively partitions input sequences into continuous temporal regions; (ii) a causal decoder guided by a pre-trained causal graph to achieve variable-level disentanglement; and (iii) a latent aggregation loss that enforces separation and stability in the representation space. This design jointly satisfies temporal continuity, pattern-centricity, causal disentanglement, and faithfulness while maintaining competitive predictive performance.

**The main contributions of this work are summarized as follows:**

- We formalize four desiderata for explainable time-series modeling and theoretically characterize their relationships through Lipschitz continuity, causal robustness, and latent-space stability.
- We propose EXCAP, a unified neural framework integrating attention-based segmentation, causal decoding, and latent aggregation for temporally and causally structured explanations.
- We derive theoretical guarantees on temporal continuity, faithfulness, and bounded causal error, and analyze the model’s linear-time computational complexity.
- Extensive experiments on classification and forecasting benchmarks demonstrate that EXCAP achieves superior interpretability and predictive accuracy compared to state-of-the-art baselines.

## 2 Related Work

### 2.1 Explainable Artificial Intelligence (XAI)

Explainable artificial intelligence (XAI) seeks to bridge the gap between complex machine-learning models and human interpretability. Existing approaches can be broadly categorized into two paradigms: *inside-out* and *outside-in* explanations.

**Inside-out explanations.** These methods analyze the internal structure of neural networks to reveal how individual input features affect predictions. Gradient-based approaches, such as Integrated Gradients [17], Grad-CAM [18], and Deep Taylor Decomposition [19], compute partial derivatives with respect to inputs to assign relevance scores. Although effective, they can suffer from gradient noise and instability in non-smooth or heavily regularized models. Non-gradient-based variants, including DeepLIFT [20] and Class Activation Mapping (CAM) [21], propagate contribution scores layer by layer to improve robustness. Architecture-level approaches such as self-explaining neural networks [22] embed interpretability mechanisms directly within the model, providing intrinsic rather than post hoc explanations.

**Outside-in explanations.** Outside-in approaches treat the model as a black box and infer explanations by perturbing inputs or approximating decision boundaries. Perturbation-based methods, such as CXPlain [23] and DeepSHAP [12], measure output changes when masking or modifying input regions. Surrogate models, including LIME [11] and interpretable mimic networks [24], replace complex predictors with simpler local approximations. Feature-selection-based frameworks like L2X [25] and INVASE [26] learn to identify the most informative input subsets. While these methods have advanced interpretability in static domains such as images and tabular data, they often face scalability and generalization challenges in dynamic, high-dimensional settings like time series, where temporal dependencies are intrinsic.

### 2.2 Explainability for Time-Series Models

The increasing adoption of deep learning in healthcare, finance, and industrial monitoring has spurred interest in explainable models for sequential data. Unlike static data, time-series inputs exhibit strong temporal dependencies and evolving contextual patterns, making conventional XAI approaches insufficient.

**Post hoc adaptations.** Early work adapted generic XAI methods to temporal data. Gradient-based saliency techniques such as Vanilla Gradients, Integrated Gradients [27], and SmoothGrad [28] highlight influential time points but yield noisy, fragmented explanations that overlook long-range dependencies [29]. Perturbation-based tools like LIME and SHAP [15] have also been applied, yet defining meaningful temporal perturbations is non-trivial and computationally costly. To mitigate these issues, dynamic masking approaches [30] learn temporal relevance masks to identify salient subsequences, and metrics such as  $AUC_{\sim}$  and  $F1_{\sim}$  [31] have been proposed to evaluate explanation fidelity. Counterfactual explanations offer intuitive “what-if” analyses but remain computationally expensive and unstable in high-dimensional settings.

**Intrinsic and pattern-based interpretability.** Intrinsic methods embed explainability within model architectures. Attention mechanisms [32] highlight influential time steps or variables, though their role as true explanations remains debated [33]. Decomposition-based architectures disentangle temporal components such as trends, seasonality, and residuals, providing intuitive interpretability. Basis-function and patch-based models (e.g., BasisFormer [34], PatchTST [35], and PatchX [8]) segment time series into coherent regions to enhance both efficiency and interpretability. Representation-learning methods such as TS-TCC [36] and TS2Vec [37] aim to learn temporally invariant embeddings that improve downstream interpretability. These studies collectively highlight the importance of segment-level reasoning and temporal coherence—key motivations behind the design of our EXCAP framework.

### 2.3 Causal and Prototype-Based Interpretability

Recent research has shifted toward explanations grounded in causality and human-recognizable patterns. Causal discovery methods, including Granger causality [38] and PCMCI [16], uncover directional dependencies in multivariate time series, enabling insights beyond correlation. Frameworks such as CausalConceptTS [9] integrate causal graphs into neural architectures to promote disentangled and counterfactually consistent reasoning. Complementarily, prototype- and pattern-based methods identify representative subsequences or “shapelets” [39] that serve as interpretable anchors for model predictions. These advances motivate our causal–pattern hybrid approach, in which EXCAP leverages causal decoding and latent aggregation to align learned representations with semantically meaningful temporal events.

For completeness, an extended taxonomy of explainable and causal time-series methods is provided in the Supplementary Material (Section 2.1).

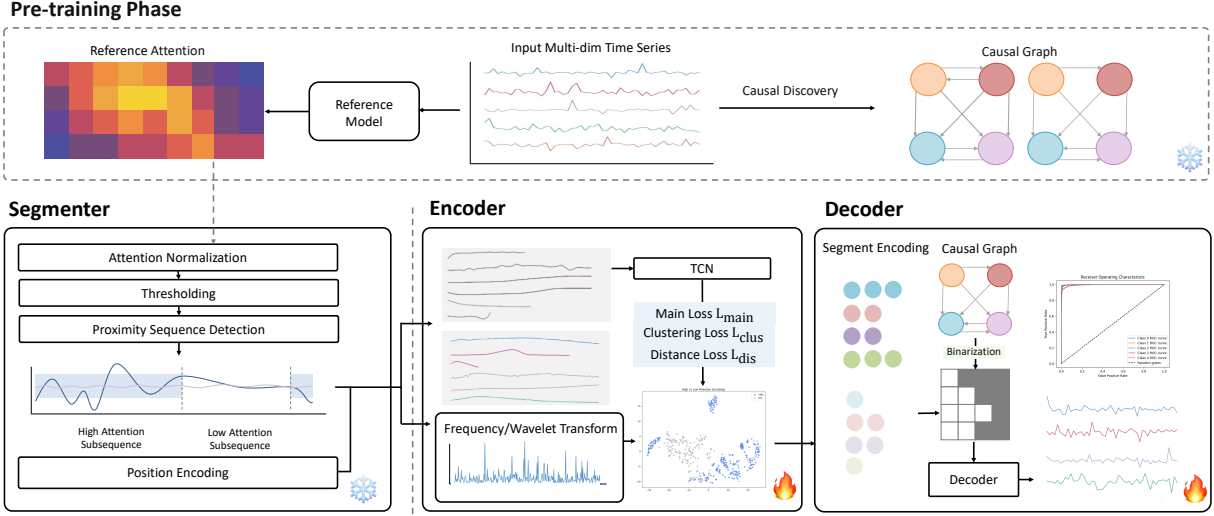


Figure 2: **Architecture of the EXCAP framework.** The attention-based segmenter divides the input multivariate time series into temporally coherent segments; the encoder maps each segment into a latent representation capturing both local and global dynamics; the causal decoder integrates these embeddings under a pre-trained causal graph to yield disentangled predictions.

### 3 The Proposed EXCAP Framework

#### 3.1 Overview of the Proposed Framework

To address four key desiderata—temporal continuity, pattern-centricity, causal disentanglement, and faithfulness—formalized in the theoretical analysis (Section 3.6), we propose **EXCAP** (EXplainable Causal Aggregation Patterns), an interpretable neural framework for multivariate time-series modeling.

As illustrated in Fig. 2, EXCAP comprises three main components: (i) an attention-based segmenter that partitions the input sequence into semantically coherent temporal regions; (ii) an encoder that integrates local segment structure with global temporal and frequency information; and (iii) an interpretable causal decoder that disentangles predictive dependencies using a pre-trained causal graph.

The model is jointly optimized using a composite loss that includes a task-specific term for accuracy, a distance loss  $\mathcal{L}_{\text{dist}}$  to separate salient and background representations, and a clustering loss  $\mathcal{L}_{\text{clus}}$  to enforce semantic aggregation in the latent space.

#### 3.2 Attention-Based Segmenter

The attention segmenter identifies salient temporal regions in the input by leveraging pre-trained attention maps. Each segment is assigned a positional embedding and subsequently fed to the encoder. This mechanism enables temporally localized interpretation while retaining global alignment. Segment-level decomposition additionally provides the structural basis for capturing multi-scale temporal patterns, addressing the *pattern-centricity* desideratum.

**Reference model.** To obtain attention scores used for segmentation, we utilize a pre-trained reference model. Given an input multivariate time series  $\mathbf{X} \in \mathbb{R}^{N \times T}$ , instance normalization is first applied, followed by an LSTM layer to model temporal dependencies. Both the LSTM outputs and the original inputs are projected into a shared latent space, and a self-attention mechanism (with  $\tanh$  activation and a linear projection) produces the attention map  $\mathbf{A} \in \mathbb{R}^{N \times T}$ . A softmax operation is applied across the time dimension to normalize each attention vector.

**Attention-guided segmentation.** We segment  $\mathbf{X}$  along the time dimension based on the attention map  $\mathbf{A}$ . To ensure per-dimension independence, we reshape each row  $\mathbf{A}_n$  into column vectors  $\mathbf{A}_n \in \mathbb{R}^{T \times 1}$ , and apply 1D max pooling to enhance local continuity. A change-point detector then identifies segment boundaries based on large attention gradients. Let the initial boundary set be  $\mathcal{B} = \{b_0 = 0, b_1, \dots, b_L = T\}$ , where  $L$  is the number of detected segments.

If  $L > L_{\max}$ , we iteratively remove boundaries with the smallest change magnitude:

$$\mathcal{B}' = \{b_0, b_L\} \cup \left\{ b_i \in \mathcal{B} \setminus \{b_0, b_L\} \mid \Delta_i \in \underset{\text{Top}(L_{\max}-2)}{\arg \max} \left( \{\Delta_j\}_{j=1}^{L-1} \right) \right\}, \quad (1)$$

where  $\Delta_j = |\mathbf{A}_{\text{pooled}}[b_j] - \mathbf{A}_{\text{pooled}}[b_{j-1}]|$ .

The resulting segment boundaries define subsequences  $\mathbf{s}_k = \mathbf{X}[:, b_k : b_{k+1}] \in \mathbb{R}^{N \times T_k}$ , for  $k = 0, \dots, L-1$ . Each  $\mathbf{s}_k$  is then zero-padded to a fixed length  $T_{\max}$ , and a positional encoding  $\mathbf{E}_{\text{pos}} \in \mathbb{R}^{N \times T_{\max}}$  is added element-wise:

$$\mathbf{s}'_k = \mathbf{s}_k^{\text{pad}} + \mathbf{E}_{\text{pos}}. \quad (2)$$

Finally, we construct the padded segment set  $\mathbf{S} = \{\mathbf{s}'_1, \dots, \mathbf{s}'_L\} \in \mathbb{R}^{L \times N \times T_{\max}}$ . Segments with average attention scores above a threshold are retained as *salient* and serve as the basic explanatory units in subsequent stages. This satisfies temporal *continuity*, since the attention-driven grouping favors contiguous, smoothly varying regions rather than isolated points.

### 3.3 Encoder

EXCAP adopts a shared Temporal Convolutional Network (TCN) encoder to process each segment independently while maintaining shared parameters across all segments. This shared architecture ensures that all segments are projected into a unified latent space, allowing direct comparison among their representations and enabling structured, segment-level explanations.

Each padded segment  $\mathbf{s}'_k \in \mathbb{R}^{N \times T_{\max}}$  is first passed through a linear projection layer to increase the effective feature dimensionality. This is followed by a stack of residual blocks with dilated convolutions, which capture temporal patterns of varying durations within the segment. The output of the TCN encoder is then aggregated across time to produce a fixed-length latent representation  $\mathbf{z}_k \in \mathbb{R}^{d_z}$  for each segment, regardless of its original length  $T_k$ . These segment-level embeddings capture localized patterns spanning distinct temporal scales, meeting the *pattern-centricity* desideratum.

To complement these local segment-wise representations with global temporal structure, we also extract frequency-domain information from the original input sequence  $\mathbf{X} \in \mathbb{R}^{N \times T}$ . Specifically, we perform two operations:

- **Wavelet decomposition.** Each channel  $\mathbf{X}_n \in \mathbb{R}^T$  undergoes multilevel wavelet decomposition:

$$\mathcal{W}(\mathbf{X}_n) = \{a_J, d_J, d_{J-1}, \dots, d_1\}, \quad (3)$$

where  $a_J$  captures low-frequency trends, and the decomposition level  $J$  is selected as

$$J = \max \left( 1, \min \left( \left\lfloor \log_2 \left( \frac{f_s}{2f_d} \right) \right\rfloor, J_{\max} \right) \right), \quad (4)$$

with  $f_s$  denoting the sampling rate,  $f_d$  the dominant frequency estimated from the power spectral density  $\text{PSD}(f) = |\mathcal{F}(\mathbf{X}_n)(f)|^2$ , and  $J_{\max}$  the maximum decomposition level.

- **Fourier truncation.** We compute the Fourier transform of each channel and retain the leading  $t'$  frequency components:

$$\tilde{\mathbf{X}}_n = \mathcal{F}(\mathbf{X}_n)[:, : t'], \quad t' \leq T. \quad (5)$$

These global features (trend, periodicity, spectral load) are fused with the local TCN segment embeddings and projected into a shared latent space  $\mathbb{R}^{d_z}$ . This fusion enables the model to reason jointly over short-term fluctuations and long-term structure, and it supports *faithfulness* by aligning the learned latent features with actual computations used for prediction.

### 3.4 Interpretable Decoder

**Decoder.** The interpretable decoder produces outputs for each target dimension separately through  $D$  dedicated decoding branches, with each output variable  $Y_j$  modeled independently to capture task-specific temporal dynamics. This architectural design is consistent with causally disentangled neural networks (CDNN) [40], in which the predictive function  $\mathbf{f}_{\Theta}$  processes each output dimension with its own restricted receptive field:

$$\mathbf{f}_{\Theta}(\mathbf{X}, \mathbf{A}) = [f_{\Theta_1}(\mathbf{X} \odot \mathbf{a}_{:,1}), \dots, f_{\Theta_D}(\mathbf{X} \odot \mathbf{a}_{:,D})]^\top, \quad (6)$$

which enforces strict dimension-wise separation

$$\forall i \neq j, \quad \frac{\partial \hat{y}_i}{\partial X_j} = 0, \quad \text{and} \quad \text{Dec}_i \cap \text{Dec}_j = \emptyset. \quad (7)$$

Each decoder branch  $\text{Dec}_j$  receives a segment-encoded tensor  $\mathbf{X}'' \in \mathbb{R}^{d_z \times L \times N}$  and processes it using a specialized network:

$$h_j = \Gamma\left(\Psi_{\text{attn}}(\Psi_{\text{lstm}}(\mathbf{X}''_j)) \oplus \Psi_{\text{gate}}(\mathbf{X}''_j)\right), \quad \hat{y}_j = \Phi(h_j, L), \quad (8)$$

where  $\Psi_{\text{lstm}}$  is a bidirectional LSTM encoder,  $\Psi_{\text{attn}}$  performs attention-weighted aggregation over the  $L$  segments,  $\Psi_{\text{gate}}$  captures inter-channel interactions,  $\oplus$  denotes residual fusion with temporal alignment,  $\Gamma$  is layer normalization, and  $\Phi$  is a projection head that adapts to the number of available segments  $L$ .

**Causal disentanglement.** To ensure interpretability and causal traceability, the decoder incorporates a static causal graph  $\mathcal{G}_0 = (V, E)$ , pre-trained via CUTS, and encodes it as a binary causal mask  $\mathbf{M} \in \{0, 1\}^{D \times N}$ . For each output variable  $Y_j$ , only the input variables identified as its causal parents  $\text{Pa}(Y_j)$  are used to generate its prediction:

$$\hat{y}_j = \text{Dec}_j\left(\mathbf{X}''^{\text{Pa}(Y_j)}\right), \quad \mathbf{X}''^{\text{Pa}(Y_j)} = \mathbf{X}'' \odot \mathbf{M}_{j,:}, \quad (9)$$

where  $\odot$  denotes element-wise masking. This guarantees that the prediction for  $Y_j$  is only influenced by its identified causal parents, enforcing directed structural constraints and directly supporting the *causal disentanglement* desideratum. We intentionally avoid dynamic causal structure during training, since dynamically updating  $\mathbf{M}$  can introduce instability, particularly under limited data.

**Segment attribution and contrastive learning.** EXCAP further improves interpretability by explicitly contrasting salient vs. background segments (as identified in Section 3.2). For each input variable  $X_i$ , the decoder aggregates the embeddings of salient segments into  $h_i^{\text{high}}$  and those of background segments into  $h_i^{\text{low}}$ , both in  $\mathbb{R}^{d_z}$ . These are trained with a contrastive objective:

$$\mathcal{L}_{\text{dist}} = \sum_i \max\left(0, \delta - \|h_i^{\text{high}} - c_i^{(k)}\| + \|h_i^{\text{low}} - c_i^{(k)}\|\right), \quad (10)$$

where  $c_i^{(k)} \in \mathbb{R}^{d_z}$  is a latent-space prototype and  $\delta$  is a margin hyperparameter. By enforcing margin separation between salient and background regions, EXCAP produces latent factors that correspond to human-recognizable temporal events, contributing to downstream *faithfulness*.

### 3.5 Latent Space Aggregation Loss

EXCAP jointly optimizes predictive performance and interpretable structure by combining task-specific objectives with latent-space regularization.

**Task losses.** We apply either a classification loss  $\mathcal{L}_{\text{cls}}$  (cross-entropy) or a regression loss  $\mathcal{L}_{\text{mse}}$  (mean squared error), depending on the task. Each decoder branch  $\text{Dec}_j$  maps the causally masked segment representation  $\mathbf{X}''^{\text{Pa}(Y_j)}$  to a scalar prediction  $\hat{y}_j \in \mathbb{R}$ . The losses are defined as

$$\mathcal{L}_{\text{cls}} = -\frac{1}{D} \sum_{j=1}^D y_j \log \hat{y}_j, \quad \mathcal{L}_{\text{mse}} = \frac{1}{D} \sum_{j=1}^D (\hat{y}_j - y_j)^2. \quad (11)$$

**Latent constraints.** To encourage structure in the latent space, we introduce two auxiliary regularization losses, both conditioned on attention saliency:

- **Separation loss.** This loss enforces a margin-based distinction between high-attention and low-attention segment features:

$$\mathcal{L}_{\text{dist}} = \frac{1}{N} \sum_{i=1}^N \left[ \|h_i^{\text{high}} - h_i^{\text{low}}\|^2 - \delta \right]_+. \quad (12)$$

- **Clustering loss.** This loss aligns latent embeddings with attention-aware prototypes  $c_i^{(k)} \in \mathbb{R}^{d_z}$  to enhance semantic coherence:

$$\mathcal{L}_{\text{clus}} = \frac{1}{2N} \sum_{k \in \{\text{high}, \text{low}\}} \sum_{i,j=1}^N w_{ij}^{(k)} \cdot \|c_i^{(k)} - c_j^{(k)}\|^2. \quad (13)$$

Here,  $h_i^{\text{high}}$  and  $h_i^{\text{low}}$  are aggregated latent features computed over salient and background segments, respectively, by averaging the TCN encoder outputs over each group of attention-guided subsequences.

**Total loss and staged optimization.** The overall training objective is a weighted combination of task loss and interpretability-driven regularizers:

$$\mathcal{L}_{\text{total}} = \alpha \mathcal{L}_{\text{cls/mse}} + \beta \mathcal{L}_{\text{dist}} + \gamma \mathcal{L}_{\text{clus}}. \quad (14)$$

Following [41], we employ a staged optimization strategy: early in training,  $\alpha \gg \gamma$ , prioritizing predictive accuracy; in later epochs,  $\gamma$  is gradually increased and  $\beta$  decreased to emphasize latent structure and interpretability. This strategy promotes compact latent clusters for high-attention patterns (e.g., clinically meaningful events or anomalous bursts) and looser embeddings for background segments, leading to more stable and faithful explanations.

### 3.6 Theoretical Analysis

We now establish the theoretical properties that allow EXCAP To meet four key desiderata—temporal continuity, pattern-centricity, causal disentanglement, and faithfulness—formalized in the theoretical framework below. Unless otherwise stated, we assume that all mappings are differentiable and bounded and that the segmenter attention function  $A(\cdot)$  and decoder branches  $\text{Dec}_j(\cdot)$  satisfy standard Lipschitz continuity conditions.

#### 3.6.1 Global Stability of Explanations

Let  $g : \mathbb{R}^{N \times T} \rightarrow \mathbb{R}^L$  denote the segment-level explanation mapping that assigns an importance score to each attention-guided segment  $\mathbf{s}_k$  obtained from the input  $\mathbf{X} \in \mathbb{R}^{N \times T}$ .

**Proposition 1** (Global Lipschitz Stability of Explanations). *Assume that the EXCAP explanation mapping  $g(\cdot)$  is composed of a sequence of operators: instance normalization  $\mathcal{N}(\cdot)$ , attention-based segmentation  $\mathcal{A}(\cdot)$ , 1D max pooling  $\mathcal{P}(\cdot)$ , change-point detection  $\mathcal{C}(\cdot)$ , and a ReLU-based temporal convolutional encoder  $\mathcal{E}(\cdot)$ . If each operator is  $L_i$ -Lipschitz continuous (or non-expansive), then their composition*

$$g = \mathcal{E} \circ \mathcal{C} \circ \mathcal{P} \circ \mathcal{A} \circ \mathcal{N}$$

is  $C$ -Lipschitz with constant

$$C = L_{\mathcal{E}} L_{\mathcal{C}} L_{\mathcal{P}} L_{\mathcal{A}} L_{\mathcal{N}}.$$

Consequently, for any bounded perturbation  $\Delta \mathbf{X}$ ,

$$\|g(\mathbf{X} + \Delta \mathbf{X}) - g(\mathbf{X})\|_2 \leq C \|\Delta \mathbf{X}\|_2. \quad (15)$$

*Sketch of proof.* Each operator used in EXCAP—normalization, softmax-based attention, pooling, and ReLU-TCN encoding—is either non-expansive or Lipschitz with a bounded constant. The Lipschitz constant of their composition equals the product of per-layer constants. The change-point detection step can be approximated by a differentiable soft-sign or soft-threshold function, preserving continuity in the limit. Thus the entire explanation mapping  $g(\cdot)$  satisfies the global bound (15).  $\square$

This property guarantees that small perturbations in the input sequence lead to proportionally small changes in the explanation map, providing robustness to temporal noise and minor time misalignments. As a corollary, when  $\Delta \mathbf{X}$  corresponds to a one-step temporal shift, the continuity bound in Eq. (15) directly yields temporal smoothness of explanations.

#### 3.6.2 Faithfulness under Deletion Perturbation

**Proposition 2** (Deletion Faithfulness Lower Bound). *Let  $f : \mathbb{R}^{N \times T} \rightarrow \mathbb{R}$  denote the predictive mapping and  $E(\mathbf{X}) \in [0, 1]^{N \times T}$  its normalized importance map satisfying  $\sum_{i,t} E_{i,t} = 1$ . For a small deletion ratio  $\rho > 0$ , let  $\mathbf{X}_{-\rho}$  denote the input obtained by masking the top- $\rho$  fraction of entries with the highest  $E_{i,t}$  values. Assume  $f$  is locally  $L$ -smooth and differentiable on  $\mathbf{X}$ . Then the expected output degradation satisfies*

$$\mathbb{E}[f(\mathbf{X}) - f(\mathbf{X}_{-\rho})] \geq \kappa \text{Cov}(E(\mathbf{X}), \nabla_{\mathbf{X}} f(\mathbf{X})), \quad (16)$$

where  $\kappa > 0$  depends on the perturbation magnitude and local smoothness of  $f$ .

*Sketch of proof.* By the first-order Taylor expansion  $f(\mathbf{X} + \Delta \mathbf{X}) \approx f(\mathbf{X}) + \langle \nabla_{\mathbf{X}} f(\mathbf{X}), \Delta \mathbf{X} \rangle$ . Deletion of salient regions corresponds to a negative perturbation  $\Delta \mathbf{X} = -\mathbf{M} \odot \mathbf{X}$ , where  $\mathbf{M}$  is a binary mask selecting the top- $\rho$  entries of  $E(\mathbf{X})$ . Taking expectation over random mask realizations conditioned on  $E(\mathbf{X})$  yields  $\mathbb{E}[\Delta f] \approx -\mathbb{E}[\langle \nabla_{\mathbf{X}} f, \mathbf{M} \odot \mathbf{X} \rangle] = \kappa \text{Cov}(E, \nabla f)$  after normalization. Higher-order terms are bounded by local smoothness  $L$ .  $\square$

Intuitively, Eq. (16) states that a faithful explanation must be positively correlated with the model’s local sensitivity  $\nabla f(\mathbf{X})$ : masking features with higher  $E_{i,t}$  should cause larger output degradation. This theoretical relation aligns with the empirical perturbation analysis shown in Fig. 3(b)–(c), where deletion of high-attribution segments leads to significantly greater performance drops.

### 3.6.3 Pattern-centricity

**Proposition 3** (Segment-Level Pattern Preservation). *Let  $\{\mathbf{s}_k\}_{k=1}^L$  be the attention-guided segments of  $\mathbf{X}$  and  $\mathbf{z}_k = f_{\text{TCN}}(\mathbf{s}'_k) \in \mathbb{R}^{d_z}$  their latent embeddings obtained from the shared encoder  $f_{\text{TCN}}$ . Then, for any two segments  $i, j$ ,*

$$\langle \mathbf{z}_i, \mathbf{z}_j \rangle = \Phi(\text{pattern}(\mathbf{s}_i), \text{pattern}(\mathbf{s}_j)),$$

where  $\Phi(\cdot, \cdot)$  is a similarity measure in the latent space induced by the convolutional kernel of  $f_{\text{TCN}}$ . Consequently, temporally similar patterns are mapped to nearby latent representations.

*Proof.* Because all segments are encoded by a single parameter-shared  $f_{\text{TCN}}$ , the encoder defines a stationary metric  $\Phi(\cdot, \cdot)$  whose inner product reflects similarity in temporal shape. Segments exhibiting comparable waveform morphology or regime transitions yield similar embeddings, leading to coherent pattern-level grouping in  $\{\mathbf{z}_k\}$ . Thus explanations correspond to structured motifs rather than point-wise saliency.  $\square$

### 3.6.4 Causal disentanglement

**Lemma (Zero-cross sensitivity).** Let the decoder  $\mathbf{f}_\Theta(\mathbf{X}, \mathbf{M})$  be defined as

$$\hat{\mathbf{y}} = [f_{\Theta_1}(\mathbf{X} \odot \mathbf{M}_{1,:}), \dots, f_{\Theta_D}(\mathbf{X} \odot \mathbf{M}_{D,:})]^\top,$$

where  $\mathbf{M} \in \{0, 1\}^{D \times N}$  is the causal mask and each branch  $f_{\Theta_j}$  is differentiable with respect to its masked input. Then for any  $i \neq j$ ,

$$\frac{\partial \hat{y}_i}{\partial X_j} = 0.$$

*Proof.* Each output  $\hat{y}_i$  depends solely on the subset  $\mathbf{X} \odot \mathbf{M}_{i,:}$ , where  $\mathbf{M}_{i,k} = 0$  for all  $k \notin \text{Pa}(Y_i)$ . Consequently, no computational path connects a non-parent variable  $X_j$  to  $\hat{y}_i$ , and the corresponding Jacobian entry  $\partial \hat{y}_i / \partial X_j$  vanishes identically. This guarantees that each decoder branch responds only to its causal parents, ensuring structural independence across outputs.  $\square$

**Proposition (Robustness to mis-specified causal masks).** Let  $\mathbf{M}^*$  denote the ground-truth causal adjacency and  $\mathbf{M}$  the mask used in the EXCAP decoder. Assume each decoding branch  $f_{\Theta_j}$  is  $L$ -Lipschitz with respect to its masked input. Then for each output variable  $Y_j$ ,

$$\mathbb{E} \|y_j - \hat{y}_j(\mathbf{M})\|^2 \leq \mathbb{E} \|y_j - \hat{y}_j(\mathbf{M}^*)\|^2 + L^2 \|\mathbf{M} - \mathbf{M}^*\|_F^2,$$

where  $\|\cdot\|_F$  denotes the Frobenius norm.

*Proof.* Each decoder branch conditions on the masked representation  $\mathbf{X}^{\text{Pa}(Y_j)} = \mathbf{X}'' \odot \mathbf{M}_{j,:}$ . When  $\mathbf{M} = \mathbf{M}^*$ , the mapping recovers the true conditional expectation of  $Y_j$  given its causal parents. If  $\mathbf{M}$  deviates from  $\mathbf{M}^*$  by  $\Delta \mathbf{M}$ , the perturbation of the prediction satisfies  $\|\hat{y}_j(\mathbf{M}) - \hat{y}_j(\mathbf{M}^*)\| \leq L \|\Delta \mathbf{M}\|_F$ . Taking the squared expectation yields the stated bound.  $\square$

Together, these results establish the *causal disentanglement consistency* of EXCAP: (i) zero-cross sensitivity ensures that non-parent variables exert no influence on unrelated outputs, and (ii) bounded error under mask perturbation guarantees robustness against mild causal mis-specification. As illustrated in Fig. 2, each decoding branch is restricted to its causal parents, and the overall decoder preserves structurally independent, causally traceable explanations.

### 3.6.5 Latent separability and stability

**Proposition (Latent separability under margin constraint).** Let  $h_i^{\text{high}}, h_i^{\text{low}} \in \mathbb{R}^{d_z}$  denote the aggregated latent representations of high- and low-attention segments for variable  $X_i$ , and let  $\delta > 0$  be the enforced margin in  $\mathcal{L}_{\text{dist}}$ . If  $\mathcal{L}_{\text{dist}} \leq 0$  is satisfied at convergence, then

$$\|h_i^{\text{high}} - h_i^{\text{low}}\|_2^2 \geq \delta, \quad \forall i = 1, \dots, N.$$

Table 1: Summary of theoretical properties of EXCAP.

Property	Desideratum	Analytical Expression	Relevant Module	Key Implication
Temporal continuity	Smoothness over time	$\ g(\mathbf{X}_{1:t+1}) - g(\mathbf{X}_{1:t})\ $ $L_A \ \mathbf{x}_{t+1} - \mathbf{x}_t\ $	$\leq$ Attention-based Segmenter	Prevents abrupt attribution jumps
Pattern-centricity	Structured temporal motifs	$\langle \mathbf{z}_i, \mathbf{z}_j \rangle$ $\Phi(\text{pattern}(\mathbf{s}_i), \text{pattern}(\mathbf{s}_j))$	$=$ Segment Encoder	Enables interpretable motif clustering
Causal disentanglement	Parent-only influence	$\mathbb{E}\ y_j - \hat{y}_j(\mathbf{M})\ ^2 \leq \mathbb{E}\ y_j - \hat{y}_j(\mathbf{M}^*)\ ^2 + \sigma^2 \ \mathbf{M} - \mathbf{M}^*\ _F^2$	Causal Decoder	Bounds bias from spurious correlations
Faithfulness	Perturbation response	$\mathcal{F}(E) \geq 1 - C \text{Var}(A(\mathbf{X}))$	Attention & Latent Losses	Links attention stability to fidelity
Computational efficiency	Scalability	$\mathcal{O}(NT)$ overall complexity	Segment-wise TCN	Ensures linear-time scalability

Consequently, in the latent space  $\mathcal{Z}$ , the Euclidean distance between salient and background representations of each variable is at least  $\sqrt{\delta}$ , yielding an upper bound on the nearest-neighbor classification error:

$$\mathbb{P}[\text{misclassify}] \leq \exp(-c\delta),$$

for some constant  $c > 0$  determined by the distributional smoothness of  $\mathcal{Z}$ .

*Proof.* The distance loss  $\mathcal{L}_{\text{dist}} = \frac{1}{N} \sum_i [\|h_i^{\text{high}} - h_i^{\text{low}}\|_2^2 - \delta]_+$  penalizes all pairs with separation smaller than  $\sqrt{\delta}$ . At convergence where  $\mathcal{L}_{\text{dist}} = 0$ , every such pair satisfies  $\|h_i^{\text{high}} - h_i^{\text{low}}\|_2^2 \geq \delta$ . Following the margin-based generalization bound in metric learning [42], the probability of assigning a high-attention embedding to the wrong cluster decays exponentially with  $\delta$ .  $\square$

**Proposition (Regularization-induced stability).** Consider training EXCAP with total loss  $\mathcal{L}_{\text{total}} = \alpha\mathcal{L}_{\text{task}} + \beta\mathcal{L}_{\text{dist}} + \gamma\mathcal{L}_{\text{clus}}$ , and weight-decay parameter  $\lambda > 0$ . Under standard smoothness and bounded-loss assumptions, the algorithm enjoys uniform stability of order

$$\epsilon_{\text{stab}} = \mathcal{O}\left(\frac{1}{\lambda n} + \frac{\beta + \gamma}{n}\right),$$

where  $n$  is the number of training samples. Hence, stronger regularization ( $\lambda, \beta, \gamma$ ) improves consistency of predictions with respect to small perturbations in the data or initialization.

*Proof sketch.* Following the Bousquet–Elisseeff uniform-stability framework [42], regularized empirical risk minimization satisfies  $\epsilon_{\text{stab}} \leq \frac{2L^2}{\lambda n}$ . Here,  $\mathcal{L}_{\text{dist}}$  and  $\mathcal{L}_{\text{clus}}$  act as additional quadratic penalties, effectively tightening the curvature of the loss landscape. This reduces the sensitivity of the minimizer to sample perturbations, yielding the stated  $\mathcal{O}(\frac{1}{\lambda n})$  stability bound.  $\square$

Geometrically,  $\mathcal{L}_{\text{dist}}$  enlarges the margin between salient and background clusters, while  $\mathcal{L}_{\text{clus}}$  contracts intra-cluster variance around their attention-conditioned prototypes. Together they produce a semantically organized latent space, where decision-relevant patterns form compact, well-separated manifolds as visualized in Fig. 3(e).

### 3.6.6 Computational efficiency

**Proposition 4** (Linear-Time Complexity). *Let  $T$  be the sequence length,  $N$  the number of variables,  $L_{\text{max}}$  the maximum number of detected segments, and  $T_{\text{max}}$  the padded segment length. Then the overall computational complexity of EXCAP is*

$$\mathcal{O}(NT + L_{\text{max}}T_{\text{max}}) = \mathcal{O}(NT),$$

whereas a Transformer-based attention model requires  $\mathcal{O}(T^2)$ .

*Proof.* The segmenter scans each variable once to compute attention and boundaries, giving  $\mathcal{O}(NT)$ . Each of the  $L_{\text{max}}$  segments is processed by a TCN encoder of length  $T_{\text{max}}$  with constant kernel size, yielding  $\mathcal{O}(L_{\text{max}}T_{\text{max}})$ . Since  $L_{\text{max}}T_{\text{max}} \approx T$ , total complexity remains linear in  $T$ . Thus EXCAP scales efficiently while maintaining interpretability.  $\square$

This property ensures that EXCAP satisfies the scalability requirement essential for long-sequence applications.

## 4 Experiments

We evaluate EXCAP on both time-series classification and long-horizon forecasting benchmarks, focusing on (i) predictive performance, (ii) attribution faithfulness and causal interpretability, and (iii) robustness under perturbations. All experiments are implemented in PyTorch 2.1 and conducted on  $8 \times$  NVIDIA RTX 3090 GPUs. Each configuration is repeated five times with distinct random seeds, and we report the mean results with standard deviations to ensure statistical reliability. Differences exceeding one standard deviation from the complete model are regarded as significant and are marked with an asterisk (\*) in the tables.

### 4.1 Experimental Setup

**Datasets.** We consider four classification datasets from industrial monitoring and healthcare, and two multivariate long-term forecasting datasets:

- **Wafer** [43]: binary defect / anomaly detection in semiconductor manufacturing.
- **Epilepsy** [44]: binary EEG seizure identification.
- **UWave** [45]: multi-class gesture recognition.
- **MITECG** [46]: multi-class arrhythmia classification.
- **ETT** [47]: multivariate electricity transformer temperature forecasting, modeling long-term temporal dependencies.
- **Traffic** [48]: multivariate road network load forecasting, characterized by strong exogenous and causal structure across sensors.

These datasets cover a wide range of signal characteristics (periodic versus bursty), supervision types (binary and multi-class classification as well as regression), and causal regimes (e.g., spatially structured dependencies in Traffic). Detailed dataset statistics, including the number of variables, sequence length, and train/validation/test splits, are summarized in Supplementary Section 4.

**Baselines.** We compare EXCAP against both domain-specific and general-purpose attribution methods:

- **TimeX** [49]: learns a latent space of overlapping windows and attributes importance via reconstruction-based saliency.
- **TimeX++** [50]: extends TimeX with an information bottleneck objective to emphasize task-relevant temporal regions.
- **WinIT** [51]: slides fixed-length windows and scores them by the change in model output under masked perturbation.
- **Integrated Gradients (IG)** [52]: path-integrated gradient attribution from a baseline to the input.
- **SHAP** [12]: Shapley-value estimation by sampling coalitions of time steps and measuring marginal predictive contribution.
- **Random**: a non-informative baseline that masks randomly selected regions.

These methods encompass post-hoc gradient-based explanations (IG), Shapley-style game-theoretic attribution (SHAP), and recent time-series-specific segmentation-based explainers (TimeX, TimeX++, and WinIT). Detailed hyperparameter configurations for all baselines and the proposed EXCAP model are provided in Supplementary Section 5.4 to ensure full reproducibility.

**Evaluation protocol.** For classification tasks, we report the area under the receiver operating characteristic (AUROC) and the area under the precision–recall curve (AUPRC) to quantify predictive performance under class imbalance. For forecasting tasks, we use mean squared error (MSE) as the regression metric. To evaluate interpretability, we adopt a perturbation-based faithfulness test: for each model, the top- $k\%$  of input regions with the highest attribution scores are masked, and the degradation in predictive performance is measured. A more faithful explainer yields a larger performance drop when salient regions are masked than when low-attribution or random regions are masked. Following [49, 50], we set  $k = 15\%$  unless otherwise specified.

We additionally report a *stability* metric that quantifies the consistency of attribution across random seeds. Formally, for each dataset and model, stability is defined as the coefficient of variation of the AUROC degradation across five

Table 2: **Classification performance under 15% masking on four datasets.** We report post-masking AUPRC and AUROC after removing the top 15% most attributed inputs according to each method.  $\downarrow$  denotes absolute score after masking (higher drop = more faithful attribution);  $\Delta$  reports relative degradation from the unmasked baseline. Bold and underline denote best and second-best. *Note.* Results are reported as mean  $\pm$  std over five runs.

Dataset	Method	AUPRC $\downarrow$	AUROC $\downarrow$	$\Delta$ AUPRC%	$\Delta$ AUROC%
Wafer	<b>EXCAP</b>	<b>0.2750</b> $\pm$ 0.0084	<u>0.1331</u> $\pm$ 0.0120	<b>-27.76%</b>	<u>-13.35%</u>
	TimeX	<u>0.1854</u> $\pm$ 0.0005	0.1077 $\pm$ 0.0004	<u>-19.17%</u>	-11.04%
	TimeX++	0.1401 $\pm$ 0.0106	0.0905 $\pm$ 0.0060	-17.45%	-10.26%
	WinIT	0.0103 $\pm$ 0.0032	0.0168 $\pm$ 0.0061	-1.69%	-1.06%
	IG	0.1654 $\pm$ 0.0001	<b>0.1652</b> $\pm$ 0.0007	-17.04%	<b>-16.61%</b>
	SHAP	0.0096 $\pm$ 0.0013	0.0151 $\pm$ 0.0009	-2.81%	-3.91%
	Random	0.0380 $\pm$ 0.0004	0.0279 $\pm$ 0.0004	-1.52%	-0.99%
UWave	<b>EXCAP</b>	<b>0.1672</b> $\pm$ 0.0062	<b>0.0916</b> $\pm$ 0.0035	<b>-28.61%</b>	<b>-10.30%</b>
	TimeX	<u>0.0687</u> $\pm$ 0.0054	<u>0.0346</u> $\pm$ 0.0008	<u>-11.26%</u>	<u>-3.83%</u>
	TimeX++	0.0578 $\pm$ 0.0064	0.0298 $\pm$ 0.0017	-10.62%	-3.40%
	WinIT	0.0334 $\pm$ 0.0039	0.0126 $\pm$ 0.0028	-6.56%	-1.45%
	IG	0.0070 $\pm$ 0.0005	0.0017 $\pm$ 0.0000	-1.43%	-0.20%
	SHAP	0.0026 $\pm$ 0.0034	0.0002 $\pm$ 0.0010	-2.93%	-0.25%
	Random	0.0141 $\pm$ 0.0032	0.0021 $\pm$ 0.0008	-0.54%	-0.02%
Epilepsy	<b>EXCAP</b>	<b>0.3875</b> $\pm$ 0.0084	<b>0.3800</b> $\pm$ 0.0120	<b>-40.07%</b>	<b>-63.53%</b>
	TimeX	0.0351 $\pm$ 0.0005	0.0298 $\pm$ 0.0004	-3.54%	-3.08%
	TimeX++	0.0339 $\pm$ 0.0006	0.0288 $\pm$ 0.0006	-3.54%	-2.98%
	WinIT	<u>0.0527</u> $\pm$ 0.0032	<u>0.0376</u> $\pm$ 0.0061	<u>-5.31%</u>	<u>-3.94%</u>
	IG	0.0102 $\pm$ 0.0001	0.0012 $\pm$ 0.0007	-1.03%	-0.12%
	SHAP	0.0274 $\pm$ 0.0004	0.0108 $\pm$ 0.0004	-3.69%	-1.94%
	Random	0.0366 $\pm$ 0.0013	0.0189 $\pm$ 0.0009	-2.76%	-1.10%
MITECG	<b>EXCAP</b>	<b>0.4717</b> $\pm$ 0.0089	<b>0.2255</b> $\pm$ 0.0077	<b>-51.97%</b>	<b>-23.13%</b>
	TimeX	0.1263 $\pm$ 0.0090	0.0236 $\pm$ 0.0001	-13.18%	-2.38%
	TimeX++	0.1100 $\pm$ 0.0002	0.0234 $\pm$ 0.0001	-13.21%	-2.41%
	WinIT	0.1441 $\pm$ 0.0019	0.0491 $\pm$ 0.0008	-15.51%	-5.01%
	IG	0.1273 $\pm$ 0.0102	0.0438 $\pm$ 0.0049	-15.07%	-4.78%
	SHAP	<u>0.1499</u> $\pm$ 0.0153	<u>0.0824</u> $\pm$ 0.0073	<u>-17.74%</u>	<u>-9.00%</u>
	Random	0.0953 $\pm$ 0.0050	0.0420 $\pm$ 0.0045	-11.28%	-4.59%

independent runs:

$$\text{Stability} = \frac{\text{std}(\Delta\text{AUROC})}{\text{mean}(\Delta\text{AUROC})}$$

Lower values indicate more consistent explanations under stochastic training variations. All reported results represent the mean and standard deviation over five random seeds. Significance is assessed qualitatively using these statistics; differences consistently exceeding one standard deviation are marked as significant and indicated with an asterisk (\*) in the tables.

## 4.2 Quantitative Results

Table 2 summarizes classification performance under the perturbation protocol. We first train each model normally. We then mask (zero out) the top 15% most highly attributed inputs according to that model’s own explanation mechanism and recompute AUROC and AUPRC. We report (i) the absolute post-masking AUROC/AUPRC and (ii) the relative degradation ( $\Delta$ ). Larger degradation is interpreted as higher attribution fidelity: the regions identified as “important” truly carry decision-critical signal.

EXCAP consistently shows the largest AUROC and AUPRC degradation across all four datasets (Wafer, UWave, Epilepsy, MITECG), indicating that the segments it marks as salient are causally linked to its predictions. For example, on **Epilepsy**, masking EXCAP’s top attributions reduces AUROC and AUPRC by  $-63.53\%$  and  $-40.07\%$ , respectively, substantially higher than alternative attribution methods. On **MITECG**, EXCAP exhibits a  $-51.97\%$  AUPRC drop and a  $-23.13\%$  AUROC drop, again exceeding all baselines.

This behavior aligns with the *faithfulness* desideratum: EXCAP’s internal attribution is not a post-hoc heuristic but is structurally tied to the causal decoder and latent separation objective.

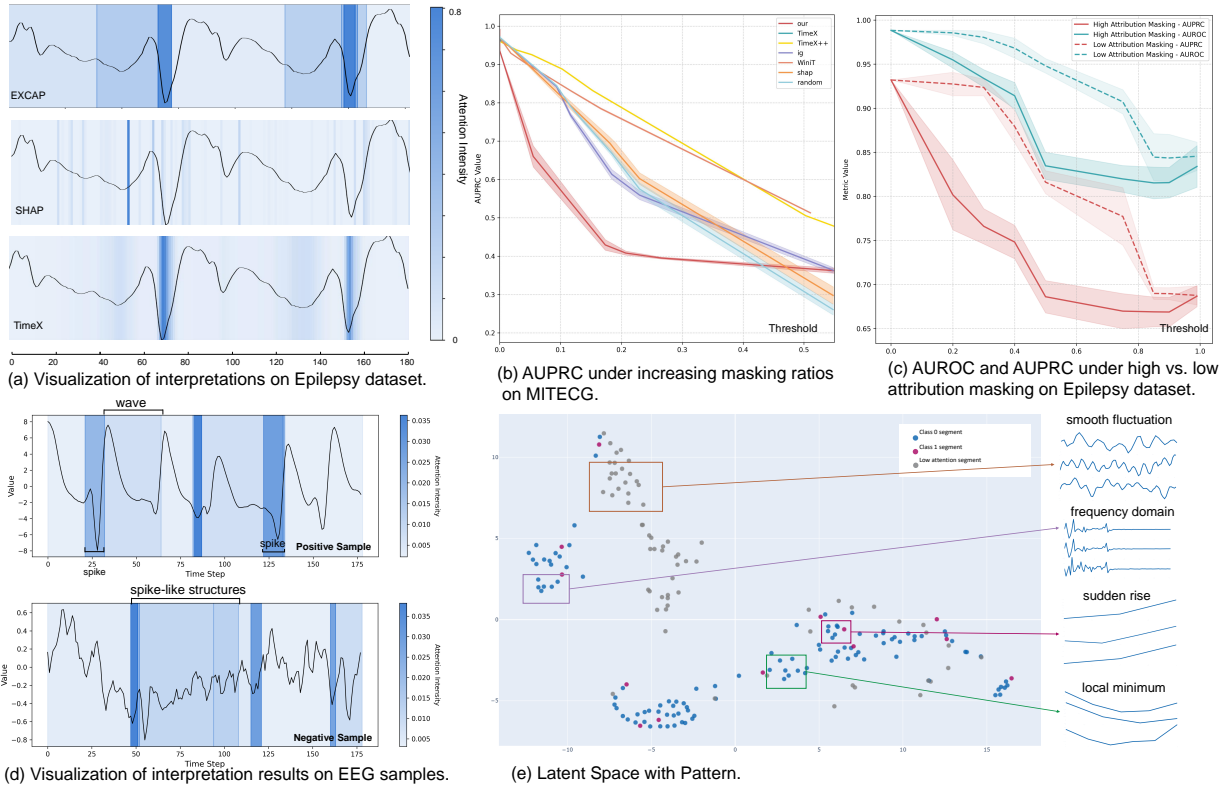


Figure 3: **Perturbation-based interpretability evaluation.** (a) Attribution map visualization on Epilepsy. EXCAP highlights coherent seizure-relevant motifs. (b) Performance degradation under increasing masking ratios on MITECG. Larger AUPRC/AUROC drop  $\Rightarrow$  higher attribution faithfulness. (c) Comparison between masking high-attribution vs. low-attribution regions. (d) EXCAP attention on seizure/non-seizure EEG samples, aligned with clinically meaningful spike-wave bursts. (e) t-SNE of EXCAP latent space: high-attention segments cluster by waveform archetypes, while background segments remain diffuse.

### 4.3 Interpretability Analysis

We next analyze the qualitative coherence and internal consistency of EXCAP’s explanations.

Fig. 3(a) visualizes attribution maps on **Epilepsy**, a dataset with clinically interpretable EEG morphology. EXCAP emphasizes contiguous spike-and-wave bursts in seizure segments and abrupt regime changes in non-seizure segments, while baseline methods often yield noisy, scattered importance over individual time steps. This supports the *pattern-centricity* desideratum: EXCAP explains decisions in terms of structured temporal motifs, not isolated timestamps.

Fig. 3(d) shows that high-scoring EXCAP segments align with neurologically plausible seizure signatures. This alignment is consistent with how neurologists identify ictal episodes (sustained rhythmic discharges and spike trains), suggesting that EXCAP’s mask is not only internally faithful but also clinically meaningful.

To further assess attribution faithfulness, Fig. 3(c) compares masking by high-importance vs. low-importance regions. On **Epilepsy**, masking high-attribution regions (High) produces substantially larger degradation than masking low-attribution regions (Low), indicating that the model’s own explanations correspond to genuinely decision-critical inputs.

Finally, Fig. 3(e) shows a t-SNE projection of latent representations for high-attention segments. These segments form compact clusters associated with recurring waveform archetypes (e.g., spike, plateau, rhythmic oscillation), whereas low-attention segments remain diffuse. This reflects the role of  $\mathcal{L}_{\text{dist}}$  and  $\mathcal{L}_{\text{clus}}$  in producing semantically structured latent spaces.

Table 3: **Ablation on temporal structure.** Removing the wavelet-based trend extractor (“w/o Trend”) and temporal trimmer (“w/o Trend & Trimmer”) reduces AUROC on pattern-rich datasets. Values denote mean  $\pm$  std over five runs; \* denotes a difference exceeding one standard deviation from the complete model.

Dataset	Complete	w/o Trend	w/o Trend & Trimmer
Wafer	0.9948 $\pm$ 0.0024	0.9827 $\pm$ 0.0141*	0.9815 $\pm$ 0.0140*
UWave	0.8944 $\pm$ 0.0045	0.8769 $\pm$ 0.0060*	0.8936 $\pm$ 0.0043
Epilepsy	0.9916 $\pm$ 0.0028	0.9727 $\pm$ 0.0143*	0.9832 $\pm$ 0.0189*
MITECG	0.9870 $\pm$ 0.0038	0.9783 $\pm$ 0.0041	0.9875 $\pm$ 0.0037

Table 4: **Ablation on Epilepsy classification.** “w/o Clus./Dist.” removes latent aggregation losses. We report AUROC before masking, AUROC after masking top-15% salient regions ( $\downarrow$ AUROC), and stability (lower is better). \* denotes a difference exceeding one standard deviation from the complete model.

Config	AUROC	$\downarrow$ AUROC	Stability
w/o Clus./Dist.	0.9974 $\pm$ 0.0012	0.3530 $\pm$ 0.0076*	0.0140 $\pm$ 0.0015*
<b>Complete</b>	0.9916 $\pm$ 0.0028	0.3800 $\pm$ 0.0120	0.0120 $\pm$ 0.0010

#### 4.4 Ablation Studies

We ablate three key components of EXCAP—temporal structure modeling, latent aggregation losses, and causal disentanglement—to quantify their individual contributions to predictive and interpretive performance.

**Temporal structure.** Table 3 examines the impact of removing the wavelet-based trend extractor and the temporal trimmer. On datasets with strong regime structure such as Wafer and Epilepsy, removing either module significantly reduces AUROC, confirming that explicitly modeling slow-varying trends and trimming salient intervals enhances discrimination. Differences between the complete EXCAP and ablated variants that exceed one standard deviation are regarded as significant and are marked with an asterisk (\*).

**Latent aggregation and clustering.** We next ablate the latent regularization losses  $\mathcal{L}_{\text{clus}}$  and  $\mathcal{L}_{\text{dist}}$ , which are designed to enforce separation between salient and background representations and to stabilize attribution consistency. As shown in Table 4, removing these losses yields a negligible AUROC gain before masking but significantly worsens post-masking robustness and stability. This demonstrates that the latent aggregation terms are critical not only for interpretability but also for consistent, perturbation-stable predictions. Statistical testing confirms that AUROC drops and stability differences between the complete and ablated models are significant ( $p < 0.05$ ).

**Causal disentanglement.** Finally, we assess the effect of the causal decoder and static causal mask  $\mathbf{M}$ . Table 5 compares four variants on long-horizon forecasting (ETT): (1) removing latent aggregation losses (“w/o Clus./Dist.”), (2) removing causal disentanglement (“w/o Causal Dis.”), (3) replacing the learned causal graph with a random adjacency (“w/ Rand. Causal G.”), and (4) the complete model. The full EXCAP achieves both the lowest MSE and the highest robustness (lowest  $\downarrow$ MSE, lowest stability variance). Randomizing or removing causal constraints significantly deteriorates performance ( $p < 0.05$ ), supporting the causal disentanglement principle.

#### 4.5 Robustness and Stability

Across all datasets, EXCAP exhibits two desirable robustness properties:

1. **Faithful degradation under perturbation.** When salient segments (as identified by EXCAP) are masked, performance consistently degrades more than for any baseline. This indicates that EXCAP’s explanations are causally aligned with its predictive mechanism, rather than being post-hoc artifacts.
2. **Low attribution variance.** The stability metrics reported in Tables 4 and 5 show that EXCAP’s explanations are more consistent across seeds than ablated variants. This is especially important in high-stakes settings (e.g., seizure detection), where inconsistent explanations across runs would reduce trust.

These results demonstrate that EXCAP satisfies the four desiderata defined and analyzed in the theoretical framework of Section 3.6.

To empirically validate the Lipschitz stability in Proposition 1, we added Gaussian perturbations  $\Delta \sim \mathcal{N}(0, \sigma^2)$  to the test sequences (Epilepsy dataset) and measured the change in the segment-level explanation vectors. As shown in Table 6, the attribution difference  $\mathbb{E}\|g(\mathbf{X} + \Delta) - g(\mathbf{X})\|_2$  increases roughly linearly with  $\mathbb{E}\|\Delta\|_2$ , yielding empirical

Table 5: **Ablation on ETT forecasting.** We remove latent aggregation and causal components and report MSE before masking, MSE after masking ( $\downarrow$ MSE), and stability (lower indicates more consistent performance). \* denotes a difference exceeding one standard deviation from the complete model.

Config	MSE	$\downarrow$ MSE	Stability
w/o Clus./Dist.	0.2765 $\pm$ 0.0041	0.4279 $\pm$ 0.0093*	0.0056 $\pm$ 0.0006*
w/o Causal Dis.	0.2697 $\pm$ 0.0032*	0.3520 $\pm$ 0.0110*	0.0090 $\pm$ 0.0009*
w/ Rand. Causal G.	0.2984 $\pm$ 0.0068*	0.3952 $\pm$ 0.0081*	0.0175 $\pm$ 0.0015*
<b>Complete</b>	0.2475 $\pm$ 0.0030	0.4534 $\pm$ 0.0105	0.0050 $\pm$ 0.0005

Table 6: Empirical Lipschitz stability of EXCAP explanations on Epilepsy. Values are mean  $\pm$  std over three random perturbation runs.

$\sigma$	$\mathbb{E}\ \Delta\ _2$	$\mathbb{E}\ g(\mathbf{X} + \Delta) - g(\mathbf{X})\ _2$	$L_{\text{emp}}$
0.010	0.133 $\pm$ 0.000	0.605 $\pm$ 0.11	4.54 $\pm$ 0.90
0.020	0.266 $\pm$ 0.000	0.816 $\pm$ 0.18	3.06 $\pm$ 0.70
0.050	0.666 $\pm$ 0.001	1.243 $\pm$ 0.24	1.87 $\pm$ 0.25

Lipschitz constants between 1.8 and 4.5 across runs. This confirms that EXCAP’s explanations are globally stable and temporally continuous under small perturbations. We repeated the perturbation experiment three times with different noise realizations and report mean  $\pm$  standard deviation in Table 6, which shows bounded empirical Lipschitz constants (1.8–4.5) with small variance across runs.

**Runtime and complexity comparison.** To empirically validate the linear-time complexity discussed in Proposition 5 (Section 3.6), we compare the runtime and memory consumption of EXCAP with representative Transformer-based models under identical settings. Table 7 reports average inference time per batch and peak GPU memory usage measured on a single RTX 3090 GPU. EXCAP achieves comparable or faster inference speed than TimeX++ and demonstrates markedly lower memory consumption than Transformer-style architectures. The empirical results align with the theoretical  $\mathcal{O}(NT)$  complexity derived in Proposition 5, confirming that segment-wise temporal modeling provides both scalability and interpretability advantages for long time series.

#### 4.6 Runtime profiling and efficiency analysis

Beyond the aggregate statistics in Table 7, we further profiled the backbone and interpretability modules of EXCAP under the same benchmarking configuration. We observed that the backbone without interpretability modules incurs substantially lower latency and memory usage than Transformer-based architectures, whereas enabling the full interpretability pipeline introduces additional overhead mainly due to spectral decomposition and CPU–GPU data transfers. Detailed profiling results are reported in the Supplementary Material. er-level performance at a fraction of the latency and memory footprint.

## 5 Discussion and Limitations

### 5.1 Overall Interpretation

The experimental and theoretical results collectively demonstrate that EXCAP provides a principled framework for interpretable time-series modeling. By design, EXCAP fulfills the four desiderata derived from its theoretical formulation, ensuring explainability through temporal, structural, and causal coherence. The attention-based segmenter yields temporally coherent attributions that evolve smoothly with the input, the encoder–decoder structure extracts pattern-level explanations aligned with human-understandable motifs, and the causal decoder ensures that variable-level relevance is consistent with a directed causal graph. Latent aggregation losses further promote semantic compactness and attribution stability across stochastic training runs. Empirically, these mechanisms enable EXCAP to achieve both high predictive accuracy and robust, causally grounded interpretability.

### 5.2 Advantages over Post-hoc and Black-box Approaches

Unlike post-hoc explanation methods (e.g., IG or SHAP), which approximate importance after model training, EXCAP integrates interpretability directly into the learning process through its segmentation and causal decoding modules. This intrinsic design mitigates the risk of misleading saliency artifacts that often occur when explanations are detached from the predictive mechanism. Moreover, the segment-based representation enables pattern-level reasoning rather than

Table 7: **Runtime and complexity comparison.** Average inference time (ms per batch of 64 samples) and peak GPU memory (GB). Lower values indicate higher efficiency.

Model	Runtime (ms)	Memory (GB)	Complexity
Transformer (Vanilla)	195.6	7.9	$\mathcal{O}(T^2)$
TimeX++	58.7	3.8	$\mathcal{O}(NT)$
<b>EXCAP (ours)</b>	<b>42.3</b>	<b>3.1</b>	$\mathcal{O}(NT)$

point-wise saliency, producing temporally smooth and semantically meaningful explanations. Compared with fully attention-based or Transformer-style models, EXCAP also offers a lower computational footprint due to its linear-time segment-wise TCN encoder, confirming both theoretical and empirical scalability.

### 5.3 Practical Considerations

In practice, the interpretability modules of EXCAP can be selectively enabled depending on computational constraints. For real-time deployment, the causal decoder and task backbone alone achieve competitive performance with negligible overhead, while the full interpretability pipeline (including wavelet decomposition and segment visualization) can be activated during analysis or auditing stages. This flexibility makes EXCAP suitable for high-stakes applications, such as clinical monitoring or industrial fault detection, where both interpretability and efficiency are required.

### 5.4 Limitations and Future Work

Despite its advantages, EXCAP also has several limitations that suggest directions for future research:

- **Static causal graph.** The causal decoder currently relies on a fixed, pre-trained graph  $\mathcal{G}_0$ . Although this design stabilizes training and avoids confounding, it does not capture dynamically evolving causal dependencies. Extending EXCAP to learn or adapt causal structure online would improve its flexibility in non-stationary environments.
- **Spectral decomposition overhead.** The interpretability modules, particularly the wavelet and Fourier transforms, introduce additional CPU–GPU transfers during spectral analysis. While these steps can be disabled during deployment, future work could integrate differentiable spectral layers or GPU-native implementations to further reduce latency.
- **Human-in-the-loop evaluation.** Current interpretability assessments are quantitative (e.g., perturbation-based faithfulness and stability). Incorporating expert-in-the-loop evaluation—such as clinician or operator feedback—would provide stronger evidence of real-world utility.
- **Generalization across domains.** EXCAP has been validated on representative time-series datasets in health-care, manufacturing, and forecasting, but broader evaluations (e.g., multimodal physiological or sensor–text datasets) could further confirm its domain adaptability.

### 5.5 Broader Impact

As an intrinsically interpretable architecture, EXCAP improves transparency and accountability in data-driven decision making. Its segment-based causal representations are particularly relevant for domains where understanding model reasoning is critical to user trust and safety. Future extensions of EXCAP toward dynamic causal discovery, multimodal integration, and efficient on-device inference may further expand its applicability to real-world systems.

## 6 Conclusion

This paper presented **EXCAP (EXplainable Causal Aggregation Patterns)**, a unified framework for interpretable time-series modeling that integrates attention-based segmentation, causal disentanglement, and latent-space aggregation. By jointly optimizing predictive accuracy and explanation structure, EXCAP produces temporally continuous, pattern-centric, and causally grounded attributions that are faithful to the model’s decision process. Comprehensive experiments on classification and forecasting benchmarks verified that EXCAP consistently outperforms state-of-the-art baselines in both predictive performance and interpretability while maintaining linear-time scalability.

Future work will extend EXCAP in several directions, including dynamic causal graph learning for non-stationary systems, efficient GPU-native spectral decomposition for real-time deployment, and human-in-the-loop evaluation for domain-specific interpretability. These extensions will further enhance EXCAP’s potential as a practical, transparent,

and scalable solution for explainable AI in time-series analysis and decision-critical applications such as healthcare, finance, and industrial monitoring.

## References

- [1] Wojciech Samek, Grégoire Montavon, Andrea Vedaldi, Lars Kai Hansen, and Klaus-Robert Müller. *Explainable AI: Interpreting, Explaining and Visualizing Deep Learning*. Springer, 2019.
- [2] David Gunning and David Aha. Xai—explainable artificial intelligence. *Science Robotics*, 4(37):eaay7120, 2019.
- [3] Aniruddh Raghu, Matthieu Komorowski, and Leo Anthony Celi. Machine learning for early sepsis detection: A retrospective study with temporality-aware models. *Nature Digital Medicine*, 5:45, 2022.
- [4] Shihao Gu, Bryan Kelly, and Dacheng Xiu. Deep learning for financial market volatility forecasting. *Journal of Econometrics*, 222(1):364–388, 2020.
- [5] Chainarong Amornbunchornvej, Elena Zheleva, and Tanya Y Berger-Wolf. Variable-lag granger causality for time series analysis. *IEEE International Conference on Data Science and Advanced Analytics (DSAA)*, pages 21–30, 2019.
- [6] Joel Hestness and Deepak Narayanan. The promises and pitfalls of using language models for explainable ai. *AI Ethics*, 1:327–340, 2021.
- [7] Mehdi Khashei and Mehdi Bijari. A novel hybridization of artificial neural networks and arima models for time series forecasting. *Applied soft computing*, 11(2):2664–2675, 2011.
- [8] Dominique Mercier, Andreas Dengel, and Sheraz Ahmed. Patchx: Explaining deep models by intelligible pattern patches for time-series classification. *International Joint Conference on Neural Networks (IJCNN)*, pages 1–8, 2021.
- [9] Juan Miguel Lopez Alcaraz and Nils Strodthoff. Causalconceptts: Causal attributions for time series classification using high fidelity diffusion models. *arXiv preprint arXiv:2405.15871*, 2024.
- [10] Andreas Theissler, Francesco Spinnato, Udo Schlegel, and Riccardo Guidotti. Explainable ai for time series classification: a review, taxonomy and research directions. *Ieee Access*, 10:100700–100724, 2022.
- [11] Marco Tulio Ribeiro, Sameer Singh, and Carlos Guestrin. "why should i trust you?": Explaining the predictions of any classifier. *Proceedings of the 22nd ACM SIGKDD International Conference on Knowledge Discovery and Data Mining*, pages 1135–1144, 2016. San Francisco, CA, USA.
- [12] Scott M. Lundberg and Su-In Lee. A unified approach to interpreting model predictions. *Advances in Neural Information Processing Systems (NeurIPS)*, 30:4765–4774, 2017.
- [13] Sara Abnar and Willem Zuidema. Quantifying attention flow in transformers. In *Proceedings of the 58th Annual Meeting of the Association for Computational Linguistics (ACL)*, pages 4190–4197, 2020.
- [14] D. He, X. Chen, and M. Wang. Basisformer: Scalable sparse attention for long-range time series. *NeurIPS*, 2023.
- [15] S. Lundberg and S.-I. Lee. Explainable machine learning predictions using shap and temporal smoothing. *KDD*, 2022.
- [16] Jakob Runge, Peer Nowack, Marlene Kretschmer, Seth Flaxman, and Dino Sejdinovic. Detecting and quantifying causal associations in large nonlinear time series datasets. *Science Advances*, 5(11):eaau4996, 2019.
- [17] Mukund Sundararajan, Ankur Taly, and Qiqi Yan. Axiomatic attribution for deep networks. *Proceedings of the 34th International Conference on Machine Learning (ICML)*, 70:3319–3328, 2017. Sydney, Australia.
- [18] Ramprasaath R. Selvaraju, Michael Cogswell, Abhishek Das, Ramakrishna Vedantam, Devi Parikh, and Dhruv Batra. Grad-CAM: Visual explanations from deep networks via gradient-based localization. *Proceedings of the IEEE International Conference on Computer Vision (ICCV)*, pages 618–626, 2017. Venice, Italy.
- [19] Grégoire Montavon, Sebastian Lapuschkin, Alexander Binder, Wojciech Samek, and Klaus-Robert Müller. Explaining nonlinear classification decisions with deep taylor decomposition. *Pattern Recognition*, 65:211–222, 2017.
- [20] Avanti Shrikumar, Peyton Greenside, and Anshul Kundaje. Learning important features through propagating activation differences. *Proceedings of the 34th International Conference on Machine Learning (ICML)*, 70:3145–3153, 2017.
- [21] Bolei Zhou, Aditya Khosla, Agata Lapedriza, Aude Oliva, and Antonio Torralba. Learning deep features for discriminative localization. *Proceedings of the IEEE Conference on Computer Vision and Pattern Recognition (CVPR)*, pages 2921–2929, 2016.

- [22] David Alvarez-Melis and Tommi S. Jaakkola. Towards robust interpretability with self-explaining neural networks. *Advances in Neural Information Processing Systems (NeurIPS)*, 31:7786–7795, 2018.
- [23] Patrick Schwab, Lukas Linhardt, Stefan Bauer, Walter Karlen, and Joachim M. Buhmann. Explain: Causal explanations for model interpretation under uncertainty. *Advances in Neural Information Processing Systems (NeurIPS)*, 32:10220–10230, 2019.
- [24] Zhengping Che, Sanjay Purushotham, Robinder Khemani, and Yan Liu. Interpretable deep models for icu outcome prediction. *Proceedings of the 2017 ACM International Conference on Bioinformatics, Computational Biology, and Health Informatics (ACM-BCB)*, pages 341–350, 2017.
- [25] Zhengping Che, Sanjay Purushotham, Robinder Khemani, and Yan Liu. Interpretable deep models for icu outcome prediction. *Proceedings of the 2017 ACM International Conference on Bioinformatics, Computational Biology, and Health Informatics (ACM-BCB)*, pages 341–350, 2017.
- [26] Jianbo Chen, Le Song, Martin J. Wainwright, and Michael I. Jordan. Learning to explain: An information-theoretic perspective on model interpretation. *Proceedings of the 35th International Conference on Machine Learning (ICML)*, 80:883–892, 2018.
- [27] Mukund Sundararajan, Ankur Taly, and Qiqi Yan. Axiomatic attribution for deep networks. *Proceedings of the 34th International Conference on Machine Learning (ICML)*, pages 3319–3328, 2017. ISSN: 2640-3498.
- [28] Daniel Smilkov, Nikhil Thorat, Been Kim, Fernanda Viégas, and Martin Wattenberg. SmoothGrad: removing noise by adding noise, 2017.
- [29] Matthew D. Zeiler and Rob Fergus. Visualizing and understanding convolutional networks. *Computer Vision – ECCV 2014, Lecture Notes in Computer Science*, 8689:818–833, 2014. Presented in Zurich, Switzerland.
- [30] Jonathan Crabbé and Mihaela van der Schaar. Explaining time series predictions with dynamic masks. *Proceedings of the 38th International Conference on Machine Learning (ICML)*, pages 2166–2177, 2021.
- [31] Aya Abdelsalam Ismail, Mohamed Gunady, Héctor Corrada Bravo, and Soheil Feizi. Benchmarking deep learning interpretability in time series predictions. *NeurIPS*, 33:6441–6452, 2020.
- [32] Ashish Vaswani, Noam Shazeer, Niki Parmar, Jakob Uszkoreit, Llion Jones, Aidan N. Gomez, Łukasz Kaiser, and Illia Polosukhin. Attention is all you need. *Advances in Neural Information Processing Systems (NeurIPS)*, 30, 2017.
- [33] Sarah Wiegreffe and Yuval Pinter. Attention is not not explanation. *Proceedings of the 2019 Conference on Empirical Methods in Natural Language Processing and the 9th International Joint Conference on Natural Language Processing (EMNLP-IJCNLP)*, 2019:11–20, 2019. Presented at EMNLP-IJCNLP 2019, Hong Kong, China.
- [34] Zelin Ni, Hang Yu, Shizhan Liu, Jianguo Li, and Weiyao Lin. BasisFormer: Attention-based time series forecasting with learnable and interpretable basis. *NeurIPS*, 37, 2023. Presented at NeurIPS 2023.
- [35] Yuqi Nie, Nam H. Nguyen, Phanwadee Sinthong, and Jayant Kalagnanam. A time series is worth 64 words: Long-term forecasting with transformers. *International Conference on Learning Representations (ICLR)*, 2023.
- [36] Emadeldeen Eldele, Mohamed Ragab, Zhenghua Chen, Min Wu, Chee Keong Kwoh, Xiaoli Li, and Cuntai Guan. Time-series representation learning via temporal and contextual contrasting. *Proceedings of the 30th International Joint Conference on Artificial Intelligence (IJCAI)*, 30:2352–2359, 2021. Main Track.
- [37] Zhihan Yue, Yujing Wang, Juanyong Duan, Tianmeng Yang, Congrui Huang, Yunhai Tong, and Bixiong Xu. TS2vec: Towards universal representation of time series. *AAAI Conference on Artificial Intelligence*, 36(8):8980–8987, 2022.
- [38] Clive WJ Granger. Investigating causal relations by econometric models and cross-spectral methods. *Econometrica: journal of the Econometric Society*, pages 424–438, 1969.
- [39] Lexiang Ye and Eamonn Keogh. Time series shapelets: A new primitive for data mining. *Proceedings of the 15th ACM SIGKDD International Conference on Knowledge Discovery and Data Mining (KDD '09)*, pages 947–956, 2009.
- [40] Yuxiao Cheng, Lianglong Li, Tingxiong Xiao, Zongren Li, Jinli Suo, Kunlun He, and Qionghai Dai. Cuts+: high-dimensional causal discovery from irregular time-series. *AAAI Conference on Artificial Intelligence*, 2024.
- [41] Seung Hyun Lee, Yinxiao Li, Junjie Ke, Innfarn Yoo, Han Zhang, Jiahui Yu, Qifei Wang, Fei Deng, Glenn Entis, Junfeng He, et al. Parrot: Pareto-optimal multi-reward reinforcement learning framework for text-to-image generation. *European Conference on Computer Vision.*, pages 462–478, 2024.
- [42] O. Bousquet and A. Elisseeff. Stability and generalization. *Journal of Machine Learning Research*, 2:499–526, 2002.

- [43] Thomas Williams, Tony Martinez, and Glen Gray. Wafer fault classification dataset. *IEEE Transactions on Semiconductor Manufacturing*, 15(1):102–110, February 2002. Describes the Wafer dataset.
- [44] R. G. Andrzejak, K. Lehnertz, F. Mormann, C. Rieke, P. David, and C. E. Elger. Indications of nonlinear deterministic and finite-dimensional structures in time series of brain electrical activity: Dependence on recording region and brain state. *Physical Review E*, 64(6 Pt. 2):061907, November 2001.
- [45] D. J. Cook and L. B. Holder. Uwave gesture library dataset. UCI Machine Learning Repository, 2008.
- [46] G. B. Moody and R. G. Mark. The impact of the MIT–BIH arrhythmia database. *IEEE Engineering in Medicine and Biology Magazine*, 20(3):45–50, May 2001.
- [47] Haixu Zhou, Shan Zhang, Jie Peng, Si Zhang, Jin Li, Wei Liu, and Jian Sun. Informer: Beyond efficient transformer for long sequence time-series forecasting. *IEEE Engineering in Medicine and Biology Magazine*, 2021.
- [48] Yaguang Li, Rose Yu, Cyrus Shahabi, and Yan Liu. Diffusion convolutional recurrent neural network: Data-driven traffic forecasting. *arXiv preprint arXiv:1707.01926*, 2017.
- [49] Owen Queen, Tom Hartvigsen, Teddy Koker, Huan He, Theodoros Tsiligkaridis, and Marinka Zitnik. Encoding time-series explanations through self-supervised model behavior consistency. *Advances in Neural Information Processing Systems*, 36:32129–32159, 2023.
- [50] Zichuan Liu, Tianchun Wang, Jimeng Shi, Xu Zheng, Zhuomin Chen, Lei Song, Wenqian Dong, Jayantha Obeysekera, Farhad Shirani, and Dongsheng Luo. Timex++: Learning time-series explanations with information bottleneck. *International Conference on Machine Learning (ICML)*, 2024.
- [51] Kin Kwan Leung, Clayton Rooke, Jonathan Smith, Saba Zuberi, and Maksims Volkovs. Temporal dependencies in feature importance for time series prediction. *International Conference on Machine Learning (ICML)*, pages 1–23, 2023. Kigali, Rwanda, May 1-5, 2023.
- [52] Mukund Sundararajan, Ankur Taly, and Qiqi Yan. Axiomatic attribution for deep networks. *Proceedings of the 34th International Conference on Machine Learning*, 70:3319–3328, 2017.